Subgrid-scale modeling in solar convection simulations

By M. S. Miesch†, N. N. Mansour AND T. Hartlep

The relatively quiescent core of the sun is surrounded by an envelope of highly turbulent convection. High-resolution numerical simulations in spherical-shell geometries have revealed much about the nature of this convection zone, but global simulations cannot resolve all of the dynamically active scales. Some version of subgrid-scale (SGS) modeling is essential. Previous SGS models have employed crude eddy viscosities and diffusivities. Here we introduce more sophisticated SGS modeling strategies into global solar convection models and report preliminary results. The new SGS models include a standard Smagorinsky model (constant C_s) as well as a dynamic Smagorinsky model.

1. Introduction

It is well known that the sun is powered by nuclear fusion. Throughout most of the solar interior, the energy released by fusion reactions in the solar core is transported outward by radiation as photons diffuse through the solar plasma on a time scale of millions of years. In the outer 30% by radius of the solar interior ($r \approx 0.7$–$1\ R$ where R is the solar radius), the plasma opacity increases and radiative transport becomes less efficient. Here thermal convection ensues and transports heat to the surface of the sun, where it is radiated into space. This is the solar convection zone, which, as the driver of the solar dynamo, is ultimately responsible for solar variability and space weather.

Modeling solar convection is a formidable challenge. The solar envelope is spherical, rotating, stratified, and magnetized. Abrupt changes in the stratification give rise to relatively small-scale granulation near the surface and convective penetration into the stably-stratified radiative interior underlying the convection zone. The range of dynamical scales present is tremendous; from the depth of the convection zone, 2×10^{10} cm to the viscous dissipation scale, which is estimated to be of order 1 cm (see, e.g., Miesch 2005). The Reynolds number varies across the convective envelope, but is everywhere greater than 10^{12}.

As turbulence researchers can readily appreciate, this system is beyond the reach of direct numerical simulation (DNS). The best we can hope for is a Large-Eddy Simulation (LES) that explicitly resolves the largest scales of motion while taking into account the influence of unresolved scales through an appropriate subgrid-scale (SGS) model.

A new global solar convection code was introduced in 1999 that is designed for efficient performance on scalable parallel computing architectures (Clune *et al.* 1999). This has since become known as the ASH (anelastic spherical harmonic) code, a moniker that reflects the anelastic equations of motion and the pseudo-spectral algorithm.

By substantially increasing the resolution relative to previous global solar convection models, ASH simulations have provided unprecedented insights into the intricate convective patterns that are likely to exist in the deep solar convection zone, into the subtleties

† High Altitude Observatory, National Center for Atmospheric Research, Boulder, Colorado

of turbulent transport processes and mean flows, and into the amplification and organization of magnetic fields through hydromagnetic dynamo action (Miesch *et al.* 2000, 2006; Elliott *et al.* 2000; Brun & Toomre 2002; DeRosa *et al.* 2002; Brun *et al.* 2004; Browning *et al.* 2006). ASH has also been used to simulate turbulent convection and dynamo processes in A-type stars (Browning *et al.* 2004; Brun *et al.* 2005).

Direct comparison with observations is not easy as we cannot observe the solar interior. However, the techniques of helioseismology allow us to infer flows and thermal structure below the solar surface through frequency shifts in global acoustic oscillations and through travel-time variations in local acoustic wave fields (Christensen-Dalsgaard 2002). This is a young but vibrant discipline. ASH simulations provide essential interpretive support and guidance to ongoing helioseismic missions such as NASA's Solar and Heliospheric Observatory (SOHO) and Solar Dynamics Observatory (SDO), the latter to be launched in 2008.

Despite these successes, ASH simulations suffer from crude modeling of unresolved processes. Current SGS models are diffusive in nature with a specified viscosity ν and thermal diffusivity κ that depend on the radial dimension r, but are fixed in time. Although ASH simulations have achieved higher resolution than previous simulations of global-scale solar convection, the contribution of SGS processes is still significant.

As an example, consider the solar internal rotation profile. Doppler measurements of the longitudinally-averaged longitudinal (zonal) velocity at the surface of the sun have long indicated that the angular velocity near the solar equator is about 30% larger than it is near the poles. Helioseismic inversions have revealed that this differential rotation persists throughout the convection zone (Thompson *et al.* 2003).

The solar differential rotation is thought to be maintained by Reynolds stresses associated with the global-scale convection. Reynolds stresses, baroclinicity, and Coriolis forces also establish an axisymmetric meridional circulation that advects angular momentum, altering the mean rotation profile. In order to achieve a statistically steady state, these two processes must balance such that

$$\boldsymbol{\nabla}\cdot\mathbf{F}_{RS} = -\boldsymbol{\nabla}\cdot\mathbf{F}_{MC} \quad , \tag{1.1}$$

where $\mathbf{F}_{RS}$ and $\mathbf{F}_{MC}$ are the time-averaged fluxes of specific angular momentum induced by Reynolds stresses and meridional circulation respectively (see, e.g. Miesch 2005). In global convection simulations $\mathbf{F}_{RS}$ includes contributions from both the resolved flow and from SGS motions that must be modeled. Inaccurate SGS models would upset the dynamical balance expressed by Eq. (1.1). It is our goal to either minimize the SGS component or at least to properly model it to give a more realistic estimation of $\mathbf{F}_{RS}$.

More generally, reliable SGS models would allow us to better assess the coherent structures thought to be present in the solar convection zone and to better capture their associated turbulent transport and hydromagnetic dynamo processes.

In this summer program we have implemented two new SGS modeling procedures into the ASH code. The first is the well-known Smagorinsky model in which the turbulent viscosity is taken to be proportional to the strain rate of the resolved velocity field (Smagorinsky 1963; Pope 2000). The second is a dynamic Smagorinsky model in which the proportionality factor is allowed to vary in space and time and is computed based on the transport properties of the resolved flow (Germano *et al.* 1990, 1991; Moin *et al.* 1992). The physical basis and the numerical algorithm of the ASH code will be discussed in Section 2 and our SGS modeling strategies will be described in Section 3. Preliminary results will be presented in Section 4.

2. The ASH code

The ASH code solves the equations of fluid motion under the anelastic approximation, which may be regarded as a compromise between fully compressible and Boussinesq approaches. The compressible fluid equations are linearized about a hydrostatic spherically-symmetric reference state, assuming the Mach number of the motions is small and the background stratification remains nearly adiabatic (see, e.g., Miesch 2005). Both assumptions are well justified in the deep solar convection zone. The first-order perturbation equations are

$$\boldsymbol{\nabla}\cdot\left(\hat{\rho}\mathbf{v}\right)=0 \tag{2.1}$$

$$\hat{\rho}\left(\frac{\partial\mathbf{v}}{\partial t}+(\mathbf{v}\cdot\boldsymbol{\nabla})\mathbf{v}\right)=-\boldsymbol{\nabla}P-\rho g\hat{\boldsymbol{r}}-2\hat{\rho}(\boldsymbol{\Omega}\times\mathbf{v})+\boldsymbol{\nabla}\cdot\boldsymbol{\tau}, \tag{2.2}$$

$$\hat{\rho}\hat{T}\left(\frac{\partial S}{\partial t}+\mathbf{v}\cdot\boldsymbol{\nabla}S\right)=-\hat{\rho}\hat{T}v_r\frac{d\hat{S}}{dr}+\boldsymbol{\nabla}\cdot\mathbf{F}_h+\Phi \quad , \tag{2.3}$$

where $\mathbf{v}$ is the fluid velocity relative to a frame rotating at an angular velocity of $\boldsymbol{\Omega}$ and $\hat{\rho}$ is the mean density stratification. The equations are expressed in spherical polar coordinates r, θ, and ϕ with corresponding unit vectors $\hat{\boldsymbol{r}}$, $\hat{\boldsymbol{\theta}}$, and $\hat{\boldsymbol{\phi}}$. The reference state density, temperature, pressure, and specific entropy are denoted as $\hat{\rho}$, $\hat{T}$, $\hat{P}$, and $\hat{S}$, whereas ρ, T, P, and S denote perturbations. Dimensional cgs units are used throughout, with the reference state and the gravitational acceleration g obtained from a solar structure model. A linearized ideal gas equation of state is assumed such that

$$\frac{\rho}{\hat{\rho}}=\frac{P}{\gamma\hat{P}}-\frac{S}{C_P} \quad , \tag{2.4}$$

where $\gamma=C_P/C_V$ and C_P and C_V are the specific heats per unit mass at constant pressure and volume respectively.

SGS motions are represented by the SGS stress tensor $\boldsymbol{\tau}$, to be discussed in §3. Since the SGS models we consider are dissipative in nature, there is also a corresponding viscous heating rate Φ in the thermal energy equation (2.3). The diffusive heat flux $\mathbf{F}_h$ is given by

$$\mathbf{F}_h=\kappa_r\hat{\rho}C_P\boldsymbol{\nabla}\left(T+\hat{T}\right)+\kappa_t\hat{\rho}\hat{T}\boldsymbol{\nabla}\left(S+\hat{S}\right) \quad , \tag{2.5}$$

where κ_r is the radiative diffusivity obtained from a solar structure model. Whereas the radiative diffusivity operates on the temperature gradient, the SGS thermal diffusivity κ_t operates on the entropy gradient as is appropriate for heat transport by thermal convection.

The mass continuity equation (2.1) allows for a background density stratification (essential for solar applications) but filters out high-frequency acoustic waves that would otherwise severely limit the time step. The ASH code has the capability of solving the magneto-hydrodynamic equations of motion, but in this paper we neglect magnetic fields.

Eqs. (2.1)–(2.5) are solved using a pseudo-spectral method with spherical harmonic basis functions in the horizontal dimensions and Chebyshev basis functions in the radial dimension. Nonlinear and Coroilis terms are advanced by means of a second-order Adams-Bashforth scheme while the remaining linear terms are advanced through a semi-implicit Crank-Nicolson scheme. The continuity equation (2.1) is satisfied identically by expressing the mass flux in terms of stream functions Z and W defined such that

$$\hat{\rho}\mathbf{v}=\boldsymbol{\nabla}\times\left(Z\hat{\boldsymbol{r}}\right)+\boldsymbol{\nabla}\times\boldsymbol{\nabla}\times\left(W\hat{\boldsymbol{r}}\right) \quad . \tag{2.6}$$

The ASH code is written in Fortran 90 and parallelized using the Message Passing Interface (MPI). It has achieved high performance on a variety of scalable parallel computing architectures including the SGI Altix system at NASA Ames Research Center (Columbia), the Compaq AlphaServer at the Pittsburgh Supercomputing Center (Lemieux), and the IBM Power4+ system at the San Diego Supercomputing Center (DataStar).

3. SGS modeling

3.1. *Basic strategy*

We assume that SGS transport is diffusive in nature, so the elements of the stress tensor $\boldsymbol{\tau}$ may be written as

$$\tau_{ij} - (1/3)\delta_{ij}\tau_{kk} = -2\hat{\rho}\nu\left[\mathcal{S}_{ij} - (1/3)\left(\boldsymbol{\nabla}\cdot\mathbf{v}\right)\delta_{ij}\right] \quad , \tag{3.1}$$

where $\mathcal{S}_{ij}$ is the strain rate tensor and the turbulent viscosity is assumed to be of the form

$$\nu = \nu_0 \left(\frac{\hat{\rho}(r_t)}{\hat{\rho}}\right)^{\alpha} + C_s\Delta^2|\mathcal{S}| \quad . \tag{3.2}$$

The first term on the right-hand side of Eq. (3.2) increases with radius r for $\alpha > 0$ and is independent of time. This is the form of the viscosity profile used in all previous ASH simulations with the exception of those reported in Young *et al.* (2003), which was a preliminary investigation of the Smagorinsky model. The value of ν_0 may be estimated from mixing-length theory but in practice it is chosen to be the smallest value that yields a well-resolved solution. Here we take $\alpha = 1$.

The second term on the right-hand-side of Eq. (3.2) was introduced by Smagorinsky (1963) and is discussed for example by Pope (2000). It is derived by assuming that the production of turbulence by shear locally balances dissipation, neglecting rotation, stratification, and compressibility. In Eq. (3.2) C_S is referred to as the Smagorinsky coefficient†, $|\mathcal{S}| = (2S_{ij}S_{ij})^{1/2}$ is the strain rate, and Δ is the geometric mean of the effective grid spacing in the three spatial dimensions:

$$\Delta = \left[\frac{\pi^2 r^2 \Delta_r}{L\left(L+1\right)}\right]^{1/3} \quad , \tag{3.3}$$

where Δ_r is the radial grid spacing and L is the maximum degree of the spherical harmonic expansions.

The Smagorinsky model is implemented by specifying the value of C_S. In this paper we use $C_S = 0.0289$, which is the value derived by Lilly for homogeneous, isotropic, incompressible turbulence (see Pope 2000). Alternatively, the value of C_S may be calculated dynamically based on the local transport properties of the resolved flow. In §3.2 we describe how we accomplish this.

Since the trace of the right-hand-side vanishes, Eq. (3.1) only strictly provides a model for the traceless part of the SGS stress tensor. A separate model may in principle be applied for the trace component, τ_{kk}, which reflects the kinetic energy of the SGS motions. However, τ_{kk} may be neglected if its magnitude is much less than the gas pressure

† C_S is sometimes also referred to as the Smagorinksy constant but this is misleading terminology here because in the dynamic model described in §3.2 C_S varies with space and time.

associated with the resolved motions. We assume that this is the case and set $\tau_{kk} = 0$ in the remainder of this paper.

3.2. *Dynamic calculation of C_S*

The Smagorinsky expression in Eq. (3.2) is a model of advective momentum transport by unresolved motions. To show this explicitly, we may regard the velocity field of the simulation, $\mathbf{v}$, as a filtered version of the full velocity field $\mathbf{v}^*$ such that $\mathbf{v} = \langle \mathbf{v}^* \rangle_g$ with the brackets denoting a low-pass filtering operation that removes structure on scales smaller than the grid spacing. Then, if we neglect the ν_0 term, Eqs. (3.1) and (3.2) imply

$$\tau_{ij} = \hat{\rho} \left(\langle v_i^* v_j^* \rangle_g - v_i v_j \right) = 2\hat{\rho} C_s \Delta^2 |\mathcal{S}| \left[\mathcal{S}_{ij} - (1/3) \left(\boldsymbol{\nabla} \cdot \mathbf{v} \right) \right] \quad . \tag{3.4}$$

Eq. (3.4) may be derived by applying the filtering operation to the equations of motion for $\mathbf{v}^*$ as described in Appendix A. It is assumed here that commutation errors may be avoided or neglected and that the filtering operation incorporates a Favre-type density weighing (see Appendix A).

If Eq. (3.4) is a reliable representation of SGS stresses, then an analogous model may also apply to the resolved scales. This is the rationale behind dynamic modeling. If we refer to the first filtering operation as the grid filter, we may introduce a second low-pass filter, which we refer to as the test filter and which operates on the resolved velocity field $\mathbf{v}$. We may again decompose the velocity field and in analogy with Eq. (3.4) we can write

$$T_{ij} = \hat{\rho} \left(\left\langle \langle v_i^* v_j^* \rangle_g \right\rangle_t - \langle v_i \rangle_t \langle v_j \rangle_t \right) = 2\hat{\rho} C_s \Delta_t 2 |\tilde{\mathcal{S}}| \left[\tilde{\mathcal{S}}_{ij} - (1/3) \left(\boldsymbol{\nabla} \cdot \langle \mathbf{v} \rangle_t \right) \right] \quad , \tag{3.5}$$

where $<>_t$ denotes the application of the test filter, Δ_t is its characteristic smoothing scale and $\tilde{\mathcal{S}}_{ij}$ and $|\tilde{\mathcal{S}}|$ represent the strain rate tensor computed using $\langle \mathbf{v} \rangle_t$.

Whereas the test filter is an explicit operation on the resolved velocity field, the grid filter is implied by Eqs. (2.2) and (3.1). The SGS velocity remains undefined; we only need to know its associated Reynolds stress, which is given by Eq. (3.4).

In this paper the test filter is taken to be a spherical harmonic cutoff in which all spherical harmonic modes of degree $\ell > L_t$ are set to zero. No explicit filtering is performed in the radial dimension. The cutoff wavenumber is set to $L_t = L/2$, where L is the maximum resolved wavenumber. This method of filtering has been used successfully in channel flow (Germano *et al.* 1991; Moin *et al.* 1991) in which filtering was done in the streamwise and spanwise directions but no explicit filtering was done in the cross-stream direction.

Applying the test filter to Eq. (3.4) and subtracting it from Eq. (3.5) yields

$$\mathcal{L}_{ij} = 2\hat{\rho} C_S \Delta_t^2 \mathcal{M}_{ij} \quad , \tag{3.6}$$

where

$$\mathcal{L}_{ij} = T_{ij} - \langle \tau_{ij} \rangle_t = \hat{\rho} \left(\langle v_i v_j \rangle_t - \langle v_i \rangle_t \langle v_j \rangle_t \right) \tag{3.7}$$

$$\mathcal{M}_{ij} = |\tilde{\mathcal{S}}| \left[\tilde{\mathcal{S}}_{ij} - (1/3) \left(\boldsymbol{\nabla} \cdot \langle \mathbf{v} \rangle_t \right) \right] - \beta \langle |\mathcal{S}| \left[\mathcal{S}_{ij} - (1/3) \left(\boldsymbol{\nabla} \cdot \mathbf{v} \right) \right] \rangle_t \tag{3.8}$$

and $\beta = \Delta / \Delta_t$. The tensors $\mathcal{L}_{ij}$ and $\mathcal{M}_{ij}$ can be computed from the resolved velocity field so Eq. (3.6) may be solved for C_S. However, there are two complications. First, Eq. (3.6) is a tensor equation and each tensor element may in general give a different value for C_S. Second, $\mathcal{M}_{ij}$ is a non-linear product of derivatives and may be expected to be highly intermittent in space and time. If it approaches zero at any point, dividing Eq. (3.6) by $\mathcal{M}_{ij}$ would not give a reliable result for C_S.

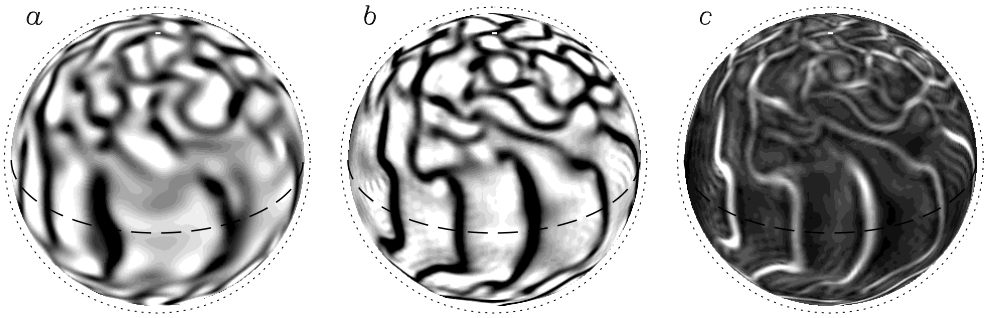

FIGURE 1. The radial velocity near the top of the shell is shown in an orthographic projection for (*a*) Case R ($C_S = 0$) and (*b*) Case DS at $t = 5.5$ and $t = 3.6$ respectively. Bright and dark tones denote upflow and downflow respectively. The north pole is tilted 35° toward the line of sight to illustrate the disparity between polar and equatorial convective patterns. The corresponding eddy viscosity in Case DS is also shown (*c*). Peak radial velocity amplitudes in these images are of order 50 m s^{-1} (*a*, *b* use the same gray scale) and the peak value of ν_s in *c* is $3.2{\times}10^{12}$ cm^2 s^{-1}.

The first complication may be overcome by selecting the value of C_S that minimizes the squared difference

$$Q = (\mathcal{L}_{ij} - 2\hat{\rho} C_S \Delta_t^2 \mathcal{M}_{ij})^2 \tag{3.9}$$

summed over all the matrix elements. This was first suggested by Lilly (1992). By setting $\partial Q / \partial C_S = 0$ we obtain

$$C_S \Delta_t^2 = -\frac{1}{2\hat{\rho}} \frac{\mathcal{L}_{ij} \mathcal{M}_{ij}}{\mathcal{M}_{ij} \mathcal{M}_{ij}} \quad , \tag{3.10}$$

where again a summation over i and j is implied. At this value of C_S it is straightforward to show that $\partial^2 Q / \partial C_S^2 > 0$ so Q is indeed minimized.

The second complication referred to above regarding the intermittency of $\mathcal{M}_{ij}$ may be avoided by averaging the numerator and denominator of Eq. (3.10) before dividing them. In this paper we average over horizontal surfaces so C_S is a function of radius and time alone. Similar approaches have been used previously in channel flow where averaging of the numerator and denominator was performed over planes parallel to the boundaries (Germano *et al.* 1991; Moin *et al.* 1991). The rationale behind this is that these dimensions are relatively homogeneous compared to the dimension perpendicular to the boundary. In the sun there is some latitudinal dependence of the flow structure, but this can be neglected as a lowest-order approximation for SGS motions.

Eq. (3.10) remains unchanged even if the trace of the SGS stress tensor τ_{kk} is non-zero because $\mathcal{M}_{kk} = 0$. More generally, a separate dynamic procedure may be used to determine τ_{kk}. This will be considered in future work.

4. Preliminary results

Fig. 1*a*-*b* compares the convection patterns in a reference simulation (Case R) with no Smagorinsky component to a similar case (DS) that includes dynamic modeling. In Case R the eddy viscosity at the top of the shell is $\nu_0 = 2.2 \times 10^{13}$ cm^2 s^{-1} according to Eq. (3.2) with $C_S = 0$. In Case DS the time-independent viscosity component has been

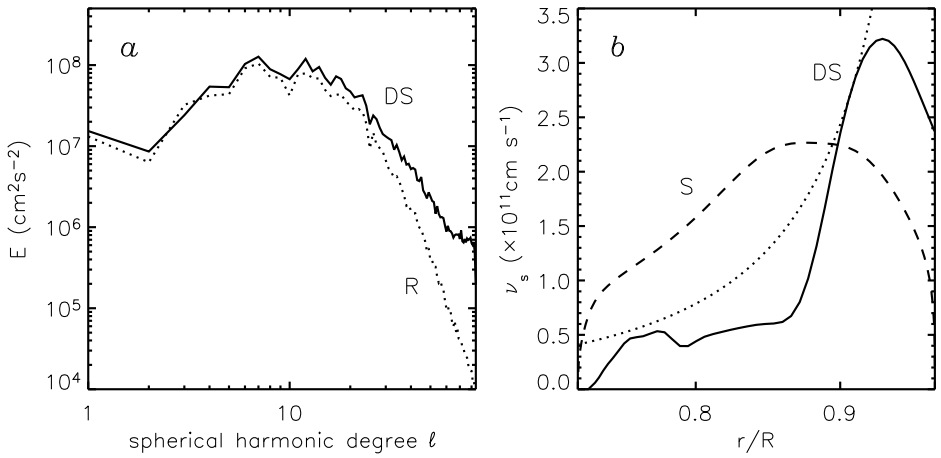

FIGURE 2. (*a*) Instantaneous power spectra of the fluctuating (non-axisymmetric) velocity component near the top of the shell in Cases R and DS, summed over longitudinal wavenumber m. The radial level and time is that shown in Fig. 1. (*b*) Amplitude of the Smagorinsky eddy viscosity component in Cases DS ($t = 1$) and S ($t = 20$) as a function of radius, averaged over horizontal surfaces. Also shown in (*b*) is the background viscosity component proportional to $\nu_0 \hat{\rho}^{-1}$ (dotted line).

reduced to $\nu_0 = 10^{12}$ cm^2 s^{-1} and C_S has been computed dynamically as described in §3.2.

Both simulations were initiated from the same state at $t = 0$. At $t = 5.5$ (Fig. 1*a*) Case R is similar to the initial state whereas Case DS is significantly different by $t = 3.6$ (Fig. 1*b*).

The striking asymmetry between upflows and downflows evident in Fig. 1 arises from the density stratification and the dramatic variation in convective patterns with latitude arises from rotation. At high latitudes, narrow downflow lanes form an interconnected network surrounding broader, weaker upflows. Near the equator, the downflow lanes align in a north-south orientation in order to minimize the inhibiting influence of Coriolis forces (see, e.g., Miesch 2005).

The downflow lanes are generally more turbulent than the upflows and this is reflected in the horizontal structure of the eddy viscosity shown in Fig. 1*c*. Downflows are fed by horizontally converging flows near the top of the shell that acquire cyclonic vorticity due to Coriolis forces. Shearing and vortex stretching instabilities within the downflows further enhance their turbulent nature.

The convective patterns in Cases R and DS are similar, although the downflow lanes in the latter are somewhat sharper and the scale of the downflow network is somewhat smaller. This is further demonstrated in Fig. 2*a* which compares the velocity spectra in these two cases. Both spectra peak at $\ell_p \sim 10$ but Case DS has more power at high wavenumbers. Case DS may also be marginally closer to power-law behavior which might signify a self-similar inertial rage. However, the presence of an inertial range is difficult to establish here due to the limited resolution; less than one decade is represented beyond ℓ_p.

Fig. 2*b* shows the Smagorinsky component of the turbulent viscosity ν_s in Case DS as a function of radius, averaged over horizontal surfaces. Also shown is ν_s for a simulation in which C_S is fixed at 0.0289 and $\nu_0 = 2 \times 10^{13}$ cm^2 s^{-1}. In the latter case, which we

refer to as Case S, the spatial dependence of ν_s is due entirely to the strain rate $|\mathcal{S}|$ which peaks near the middle of the convection zone. By contrast, ν_s in Case DS is much more strongly peaked near the top of the convection zone due to the radial dependence of C_S.

The mean amplitude of the Smagorinsky viscosity component in case DS is comparable to the ν_0 component, although ν_s can be roughly an order of magnitude larger in localized areas (cf. Fig. 1*c*). In Case S, ν_0 is an order of magnitude larger than in Case DS and it dominates the total viscosity except in localized areas. Eventually we wish to substantially reduce ν_0 such that ν_s dominates but preliminary attempts to do this have resulted in numerical instability.

5. Summary and conclusion

We have implemented two new SGS modeling strategies into numerical simulations of global-scale solar convection. The first is a conventional Smagorinsky model in which the turbulent viscosity is proportional to the strain rate of the resolved flow. The second strategy is a dynamic Smagorinsky model in which the coefficient of proportionality C_S is allowed to vary with radius and time and is computed based on the effective turbulent viscosity of resolved small-scale motions. The resulting turbulent viscosity peaks strongly in downflow lanes where vorticity and shear are maximized and near the top of the shell where velocity amplitudes are greater as a result of the density stratification.

Preliminary results look promising; the largest scales are less viscous than in previous models and power is spread over a wider range of wavenumbers for a given spatial resolution. This brings us closer to solar conditions where the Reynolds number is extremely large ($R_e \sim 10^{12}$). However, our current simulations S and DS are not numerically stable for long durations so they should be viewed as tentative. Further work is needed to identify and correct the source of instability.

Acknowledgments

We thank Alan Wray, Parviz Moin, Frank Ham, and Ugo Piomelli for enlightening discussions. We also thank Alan Wray and Matthias Rempel for reviewing the manuscript and Jean-Francois Ripoll and Ugo Piomelli for presenting aspects of this work at the summer program. The ASH simulations and code development described here and elsewhere have been done in collaboration with Juri Toomre, Sacha Brun, Matt Browning, Marc DeRosa, and Ben Brown. We appreciate their continued support both intellectually and in sharing computing resources. The simulations reported here have been carried out on the Columbia system in NASA's Advanced Supercomputing Division.

Appendix A. LES filtering and commutation errors

If we decompose the velocity field into resolved and SGS components as in §3.2, then the non-linear advection terms in the evolution equation for the full velocity field $\mathbf{v}^*$ may be written as

$$\hat{\rho}\frac{\partial \mathbf{v}^*}{\partial t} = -\hat{\rho}\left(\mathbf{v}^* \cdot \boldsymbol{\nabla}\right)\mathbf{v}^* + \ldots = \boldsymbol{\nabla}\cdot\left(\hat{\rho}\boldsymbol{A}\right) + \ldots \quad , \tag{A 1}$$

where

$$A_{ij} = v_i^* v_j^* \quad . \tag{A 2}$$

Now we define a Favre filtering operation on an arbitrary variable f as (Moin *et al.* 1991)

$$\langle f \rangle_g = \frac{\langle \hat{\rho} f \rangle_r}{\hat{\rho}} \quad , \tag{A 3}$$

where $<>_r$ denotes a filter associated with the spatial resolution. In the ASH code, $<>_r$ is a spectral cutoff filter with spherical harmonic basis functions in the horizontal dimension and Chebyshev basis functions in the vertical dimension.

Applying the grid filter to Eq. (A 1) yields

$$\hat{\rho}\frac{\partial \mathbf{v}}{\partial t} = \boldsymbol{\nabla}\cdot\left(\hat{\rho}\left\langle \boldsymbol{A}\right\rangle_g\right) + \boldsymbol{\epsilon} + \ldots = -\hat{\rho}\left(\mathbf{v}\cdot\boldsymbol{\nabla}\right)\mathbf{v} + \boldsymbol{\nabla}\cdot\boldsymbol{\tau} + \boldsymbol{\epsilon}\ldots \quad , \tag{A 4}$$

where $\mathbf{v} = \langle \mathbf{v}^* \rangle_g$ and

$$\boldsymbol{\epsilon} = \langle \boldsymbol{\nabla}\cdot(\hat{\rho}\boldsymbol{A})\rangle_g - \boldsymbol{\nabla}\cdot\left(\hat{\rho}\left\langle \boldsymbol{A}\right\rangle_g\right) \tag{A 5}$$

is the commutation error. Apart from $\boldsymbol{\epsilon}$, Eq. (A 4) is equal to Eq. (2.2) with

$$\tau_{ij} = \hat{\rho}\left(\left\langle v_i^* v_j^*\right\rangle_g - v_i v_j\right) \tag{A 6}$$

as expressed in Eq. (3.4).

Commutation errors arise from both the spherical geometry and the presence of boundaries. In a pseudo-spectral method they may also arise from the nature of the basis functions such as the Chebyshev polynomials used in ASH.

For illustration we consider the case in which $<>_r$ is a spherical harmonic filter with a cutoff wavenumber L. The commutation error may be estimated by first expressing an arbitrary function f by means of a spherical harmonic series:

$$f(r,\theta,\phi) = \Sigma_{\ell=0}^{\infty}\Sigma_{m=0}^{\ell} f_{\ell m}(r) Y_{\ell m}(\theta,\phi) \quad , \tag{A 7}$$

where $Y_{\ell m}(\theta,\phi)$ is a spherical harmonic of degree ℓ and order m. The triangular truncation $m \le \ell$ in Eq. (A 7) provides uniform resolution over horizontal surfaces.

Now we may operate on f with a linear differential operator $\mathcal{D}$ in the horizontal dimensions. The result will have its own series representation which is in general infinite even if the series for f is finite:

$$g = \mathcal{D}\{f\} = \Sigma_{\ell=0}^{\infty}\Sigma_{m=0}^{\ell} f_{\ell m}(r)\mathcal{D}\left\{Y_{\ell m}(\theta,\phi)\right\} = \Sigma_{\ell=0}^{\infty}\Sigma_{m=0}^{\ell} g_{\ell m}(r) Y_{\ell m}(\theta,\phi) \quad . \tag{A 8}$$

The spectral coefficients are given by

$$\begin{aligned} g_{\ell m} &= \int_0^{2\pi}\int_0^{\pi} g Y_{\ell m}^*(\theta,\phi)\sin\theta d\theta d\phi \\ &= \Sigma_{\ell'=0}^{\infty}\Sigma_{m'=0}^{\ell'} f_{\ell' m'}\int_0^{2\pi}\int_0^{\pi}\mathcal{D}\left\{Y_{\ell',m'}(\theta,\phi)\right\} Y_{\ell m}^*(\theta,\phi)\sin\theta d\theta d\phi \quad , \end{aligned} \tag{A 9}$$

where $Y_{\ell m}^*$ is the complex conjugate of $Y_{\ell m}$.

So far we have not applied any filtering. If we apply a spectral cutoff filter after applying the derivative operation $\mathcal{D}$, then the spherical harmonic coefficients of g will be given by Eq. (A 9) but $g_{\ell m}$ will be zero for $\ell > L$. If instead we apply the filter before the derivative operation, then the $g_{\ell m}$ will in general form an infinite series but the summation over ℓ' on the right-hand side of Eq. (A 9) will only extend to L rather than ∞.

The commutation error for this operation, $\epsilon_D(\ell, m)$ may then be expressed as

$$\epsilon_D(\ell,m) = \langle \mathcal{D}\{f\}\rangle_r - \mathcal{D}\{\langle f\rangle_r\}$$
$$= \Sigma_{\ell'=L+1}^{\infty}\Sigma_{m'=0}^{\ell'} f_{\ell' m'} \int_0^{2\pi}\int_0^{\pi} \mathcal{D}\{Y_{\ell',m'}(\theta,\phi)\}\, Y^*_{\ell m}(\theta,\phi)\sin\theta d\theta d\phi \quad . \quad \text{(A 10)}$$

The commutation error only depends on the SGS component of f, $\ell > L$, which will be small if most of the energy is in the resolved modes. Furthermore, many operations such as $\partial f/\partial\phi$ and $\sin\theta\partial f/\partial\theta$ are local in spectral space in the sense that $\mathcal{D}\{Y_{\ell m}\}$ only involves modes between $\ell-1$ and $\ell+1$. Thus, for these operators, the commutation error will vanish for the resolved velocity field where $\ell < L$ due to the orthogonality of the spherical harmonics. We have focused here on the horizontal grid filtering but similar arguments apply to the radial grid filtering and the test filtering.

Commutation errors are only relevant when justifying Eqs. (3.4) and (3.5) which relate the stress tensors τ_{ij} and T_{ij} to subfilter-scale velocity correlations. As demonstrated in this appendix, these equations are only strictly valid if commutation errors can be neglected. However, Eqs. (3.4) and (3.5) may alternatively be taken at face value, as SGS models in their own right. Then explicit filtering of the momentum equations is unnecessary and commutation errors do not arise.

REFERENCES

Browning, M. K., Brun, A. S. & Toomre, J. 2004 Simulations of core convection in rotating A-type stars: differential rotation and overshooting. *Astrophys. J.*, **601**, 512–529.

Browning, M. K., Miesch, M. S., Brun, A. S. & Toomre, J. 2006 Dynamo action in the solar convection zone and tachocline: Pumping and organization of toroidal fields. *Astrophys. J. Let.*, 648, L157–L160.

Brun, A. S. & Toomre, J. 2002 Turbulent convection under the influence of rotation: Sustaining a strong differential rotation. *Astrophys. J.* **570**, 865–885.

Brun, A. S., Miesch, M. S. & Toomre, J. 2004 Global-scale turbulent convection and magnetic dynamo action in the solar envelope. *Astrophys. J.* **614**, 1073–1098.

Brun, A. S., Browning, M. K. & Toomre, J. 2005 Simulations of core convection in rotating A-type stars: Magnetic dynamo action. *Astrophys. J.*, **629**, 461–481.

Clune, T. C., Elliott, J. R., Miesch, M. S., Toomre, J. & Glatzmaier, G. A. 1999 Computational aspects of a code to study rotating turbulent convection in spherical shells. *Parallel Computing.* **25**, 361–380.

Christensen-Dalsgaard, J. 2002 Helioseismology. *Rev. Mod. Phys.*, **74**, 1073–1129.

DeRosa, M. L., Gilman, P. A. & Toomre, J. 2002 Solar multiscale convection and rotation gradients studied in shallow spherical shells. *Astrophys. J.* **581**, 1356–1374.

Elliott, J. R., Miesch, M. S. & Toomre, J. 2000 Turbulent solar convection and its coupling with rotation: The effect of Prandtl number and thermal boundary conditions on the resulting differential rotation. *Astrophys. J.* **533**, 546–556.

Germano, M., Piomelli, U., Moin, P. & Cabot, W. H. 1990 A dynamic subgrid-scale eddy viscosity model. *Proceedings of the 1990 Summer Program*, Center for Turbulence Research, NASA Ames/Stanford Univ.

Germano, M., Piomelli, U., Moin, P. & Cabot, W. H. 1991 A dynamic subgrid-scale eddy viscosity model. *Phys. Fluids A* **3**, 1760–1765.

Lilly, D. K. 1992 A proposed modification of the Germano subgrid-scale closure method. *Phys. Fluids A* **4**, 633–635.

Miesch, M. S. 2005 Large-scale dynamics of the convection zone and tachocline. *Living Reviews in Solar Physics.* **2**, Online Journal article, http://www.livingreviews.org/lrsp-2005-1.

Miesch, M. S., Brun, A. S. & Toomre, J. 2006 Solar differential rotation influenced by latitudinal entropy variations in the tachocline. *Astrophys. J.* **641**, 618–625.

Miesch, M. S., Elliott, J. R., Toomre, J., Clune, T. C., Glatzmaier, G. A. & Gilman, P. A. 2000 Three-dimensional spherical simulations of solar convection: Differential rotation and pattern evolution achieved with laminar and turbulent states. *Astrophys. J.* **532**, 593–615.

Moin, P., Squires, K., Cabot, W. & Lee, S. 1991 A dynamic subgrid-scale model for compressible turbulence and scalar transport. *Phys. Fluids A* **3**, 2746–2757.

Pope, S. B. 2000 *Turbulent flows*. Cambridge Univ. Press.

Smagorinsky, J. 1963 General circulation experiments with the primitive equations. I. The basic experiment. *Monthly Weather Rev.* **91**, 99–164.

Thompson, M. J., Christensen-Dalsgaard, J., Miesch, M. S. & Toomre, J. 2003 The internal rotation of the sun. *Ann. Rev. Astron. Astrophys.* **41**, 599–643.

Young, Y.-N., Miesch, M. S. & Mansour, N. N. 2003 Subgrid scale modeling in solar convection simulations using the ASH code. *Annual Research Briefs 2003*, Center for Turbulence Research, NASA-Ames/Stanford Univ..